

Efficient magnon transport and magnon torque through the epitaxial antiferromagnetic insulator α-Fe_2O_3

Donglin Song(宋东霖), Fanyu Meng(孟凡毓), Mingyang Sun(孙铭扬), Hongrui Ni(倪泓睿), Jinhao Zou(邹锦豪), Zichen Yao(姚子忱), Zhenlong Guo(郭振龙), Yichi Zhang(张一驰), Liyan Zhang(张丽艳), Hongliang Bai(白洪亮), Wenping Zhou(周文平), and Yi Wang(王译)

Citation: Chin. Phys. B, 2026, 35 (**4**): 047505. DOI: 10.1088/1674-1056/ae48c1
http://cpb.iphy.ac.cn; http://iopscience.iop.org/cpb

What follows is a list of articles you may be interested in

Recent progress on electron- and magnon-mediated torques

Jia-Min Lai(来嘉敏), Bingyue Bian(边冰玥), Zhonghai Yu(于忠海), Kaiwei Guo(郭凯卫), Yajing Zhang(张雅静), Pengnan Zhao(赵鹏楠), Xiaoqian Zhang(张霄倩), Chunyang Tang(汤春阳), Jiasen Cao(曹家森), Zhiyong Quan(全志勇), Fei Wang(王飞), and Xiaohong Xu(许小红)

Chin. Phys. B, 2025, 34 (**10**): 107501. DOI: 10.1088/1674-1056/add909

Multiferroicity and thermal expansion of the layered metal-organic framework $[NH_4Cl]_2[Ni(HCOO)_2(NH_3)_2]$

Dan Cheng(程丹), Yingjie He(何英杰), Shuang Liu(刘爽), Na Su(苏娜), and Young Sun(孙阳)

Chin. Phys. B, 2025, 34 (**6**): 067505. DOI: 10.1088/1674-1056/adcaa4

A design for an antiferromagnetic material based on self-assembly for information storage

Si-Yan Gao(高思妍), Yi-Feng Zheng(郑益峰), Shu-Qiang He(何述强), Haiping Fang(方海平), and Yue-Yu Zhang(张越宇)

Chin. Phys. B, 2025, 34 (**6**): 067504. DOI: 10.1088/1674-1056/adc6f5

Complex magnetic and transport properties of $EuBi_2$ single crystal

Ping Su(苏平), Hui Liang(梁慧), Yi-Ran Li(李祎冉), Huan Wang(王欢), Na Li(李娜), Kai-Yuan Hu(胡开源), Ying Zhou(周颖), Dan-Dan Wu(吴丹丹), Yan Sun(孙燕), Qiu-Ju Li(李秋菊), Jin-Jin Hong(洪锦锦), Xia Zhao(赵霞), Xue-Feng Sun(孙学峰), and Yi-Yan Wang(王义炎)

Chin. Phys. B, 2025, 34 (**6**): 067503. DOI: 10.1088/1674-1056/adca17

Crystal structure, magnetic properties, and tunable Kondo effect in a new compound Nd_5ScSb_{12}

Yi-Ran Li(李祎冉), Na Li(李娜), Ping Su(苏平), Hui Liang(梁慧), Kai-Yuan Hu(胡开源), Ying Zhou(周颖), Dan-Dan Wu(吴丹丹), Yan Sun(孙燕), Qiu-Ju Li(李秋菊), Xia Zhao(赵霞), Xue-Feng Sun(孙学峰), and Yi-Yan Wang(王义炎)

Chin. Phys. B, 2025, 34 (**6**): 067502. DOI: 10.1088/1674-1056/adc2df

---

SPECIAL TOPIC — Advanced magnonics

Efficient magnon transport and magnon torque through the epitaxial antiferromagnetic insulator α-Fe_2O_3

Donglin Song(宋东霖)[1,2,†], Fanyu Meng(孟凡毓)[1,2,†], Mingyang Sun(孙铭扬)[1,2], Hongrui Ni(倪泓睿)[1,2], Jinhao Zou(邹锦豪)[2], Zichen Yao(姚子忱)[2], Zhenlong Guo(郭振龙)[1,2], Yichi Zhang(张一驰)[1,2], Liyan Zhang(张丽艳)[3], Hongliang Bai(白洪亮)[1], Wenping Zhou(周文平)[4], and Yi Wang(王译)[1,2,‡]

[1] *Key Laboratory of Materials Modification by Laser, Ion and Electron Beams (Dalian University of Technology), Ministry of Education, Dalian* 116024, *China*

[2] *School of Physics, Dalian University of Technology, Dalian* 116024, *China*

[3] *School of Chemical Engineering, Dalian University of Technology, Dalian* 116024, *China*

[4] *Inner Mongolia Key Laboratory of Microscale Physics and Atom Innovation, and Research Center for Quantum Physics and Technologies, Inner Mongolia University, Hohhot* 010021, *China*

(Received 20 December 2025; revised manuscript received 9 February 2026; accepted manuscript online 23 February 2026)

Magnons, as key carriers of spin angular momentum, enable spin transport without charge movement in magnetic insulators, thereby greatly reducing Joule heating in spintronic devices. Magnon-mediated spin torque (i.e., magnon torque) provides an alternative approach for efficient magnetization manipulation. However, magnon transmission through antiferromagnetic insulators still suffers from notable propagation losses, limiting the efficiency of magnon torque. Here, we fabricate high-quality epitaxial α-Fe_2O_3 thin films by magnetron sputtering that exhibit strong antiferromagnetic ordering, and successfully demonstrate highly efficient magnon transport and magnon torque in Pt/α-Fe_2O_3/NiFe devices at room temperature. It is observed that magnons propagate through a 20-nm-thick α-Fe_2O_3 layer with a significantly enhanced transmission efficiency of 75%, about 2.5 times higher than that in previously reported NiO-based magnonic devices. Consequently, a pronounced magnon torque is exerted on the adjacent ferromagnetic layer. Our work demonstrates that α-Fe_2O_3 is a promising antiferromagnetic material for efficient magnon channels, advancing the study of energy-efficient, high-speed magnonic devices.

Keywords: α-Fe_2O_3, spin-torque ferromagnetic resonance, magnon torque, efficient magnon transport

PACS: 75.76.+j, 75.50.Ee, 75.30.Ds, 76.50.+g

DOI: 10.1088/1674-1056/ae48c1 **CSTR:** 32038.14.CPB.ae48c1

1. Introduction

Magnons, the quanta of spin waves, exhibit the advantages of dissipation-free and low-damping transfer of spin information over micrometer or even millimeter-long distances in magnetic insulators without electron motion.[1–4] Moreover, magnons exhibit an inherent dynamic frequency as high as terahertz.[5,6] Therefore, magnon-based devices have great potential for low-power, high-speed signal processing and information storage, overcoming the heating and low-frequency issues in traditional electronic devices.[1,3,5,7]

The realization of practical magnonic devices fundamentally requires efficient and controllable generation, transmission, and detection (or storage) of magnon signals.[3,5,7] Recent theoretical advances have highlighted the profound influence of symmetry and lattice structure on magnon transport, as revealed in studies of antiferromagnetic topological insulators[8] and higher-order topological states in altermagnets.[9] Additionally, magnon-magnon interactions have been shown to significantly regulate topological phase transitions.[10] Previous studies have extensively focused on magnon excitation[11–15] and magnon transport in devices incorporating polycrystalline thin films of antiferromagnetic insulators, such as NiO, CoO, and Cr_2O_3.[16–19] Meanwhile, the magnon torque effect has been widely investigated based on the antiferromagnetic insulator NiO,[20–26] enabling energy-efficient magnetization control and robust magnon information readout in integrated magnonic circuits.

However, the efficiency of magnon transport in current devices remains insufficient. NiO thin films generally possess a relatively low Néel temperature and often exhibit paramagnetic behavior at room temperature. Even below the Néel temperature, the presence of up to twelve magnetic domain types in NiO[27] leads to complex multi-domain configurations, which hinder efficient magnon transport. Moreover, NiO thin films are typically polycrystalline and contain more defects and grain boundaries than single-crystal materials. These structural defects make magnons more susceptible to scattering during transport,[28] thereby shortening their

[†] These authors contributed equally to this work.

[‡] Corresponding author. E-mail: yiwang@dlut.edu.cn

© 2026 Chinese Physical Society and IOP Publishing Ltd. All rights, including for text and data mining, AI training, and similar technologies, are reserved.

mean free path and further degrading magnon transmission efficiency.

In contrast, α-Fe_2O_3 (hematite) is a promising antiferromagnetic material with a Néel temperature well above room temperature (848 K),[29] allowing its thin films to maintain antiferromagnetic order at room temperature. Furthermore, α-Fe_2O_3 has simpler magnetic domain configurations than NiO, with only three possible magnetic domain types[30] at room temperature. High-quality epitaxial α-Fe_2O_3 thin films are also more readily achievable than their NiO counterparts. It is therefore compelling to ask whether α-Fe_2O_3 thin films can exhibit higher magnon transmission efficiency and stronger magnon torque effect. These questions have remained unexplored to date.

In this work, we address the aforementioned questions by investigating magnon transport and the magnon torque effect in high-quality epitaxial α-Fe_2O_3 thin films. We, for the first time, demonstrate magnon torque in α-Fe_2O_3-ferromagnetic heterostructures and observe a significant enhancement of magnon transmission efficiency. The value is quantitatively determined to be 75%, substantially exceeding the typical efficiency of $\sim$ 30% reported for commonly used NiO. Our findings establish α-Fe_2O_3 as a superior material platform for exploring room-temperature magnonic devices.

2. Experimental details

2.1. Preparation and characterization of α-Fe_2O_3 thin films

The α-Fe_2O_3 thin films are epitaxially grown on sapphire (α-Al_2O_3) substrates using a radio-frequency magnetron sputtering technique. A high-purity (99.99%) Fe_2O_3 target (3 mm thick, 50.8 mm in diameter) is used for deposition. Before sputtering, the vacuum chamber is evacuated to a base pressure below 5×10^{-6} Pa. During deposition, the substrate temperature is maintained at 600 °C, and the sputtering power is fixed at 120 W. The chamber is filled with a mixture of Ar and O_2 at a constant working pressure of 2 mTorr, with the Ar/O_2 flow ratio systematically varied from 19.4:0.6 to 17:3.

The structural properties of the films are characterized using x-ray diffraction (XRD). Surface morphology and roughness are analyzed by atomic force microscopy (AFM), while transmission electron microscopy (TEM) is employed to examine the microstructure. Magnetic properties are measured using a vibrating sample magnetometer (VSM) within the physical property measurement system (PPMS).

2.2. Preparation and characterization of Pt/α-Fe_2O_3 heterostructures

A Pt layer is first deposited on the sapphire substrate using radio-frequency magnetron sputtering at 600 °C. The working pressure is kept at 2 mTorr, and the applied power on the target is fixed at 40 W. Subsequently, an α-Fe_2O_3 thin film is grown on the Pt layer with an optimized Ar/O_2 flow ratio of 19.2:0.8. The crystal structure and film quality of the heterostructures are analyzed by XRD and Raman spectroscopy. TEM is also used to examine the epitaxial properties and atomic-scale interface.

2.3. ST-FMR measurements

Spin-torque ferromagnetic resonance (ST-FMR) measurement is a common method used to measure spin–orbit torque (SOT) in heavy-metal/ferromagnet bilayer structures. Pt (6 nm)/α-Fe_2O_3 ($t_{\alpha-Fe_2O_3}$)/NiFe (6 nm)/SiO_2 devices with different α-Fe_2O_3 thicknesses (0–50 nm) are fabricated using photolithography and Ar-ion etching techniques. A radio-frequency current is applied to generate spin currents at the Pt/α-Fe_2O_3 interface, which subsequently induce magnon currents in the α-Fe_2O_3 layer. The resulting ST-FMR signals are detected using a lock-in amplifier to quantify the magnon torque.

3. Results and discussion

By optimizing the deposition conditions, the optimal gas flow ratio for α-Fe_2O_3 film growth was determined to be $Ar : O_2 = 19.2 : 0.8$. Detailed growth optimization and TEM image of an α-Fe_2O_3 film are provided in the supplemental material S1. The surface morphology of the film was characterized using AFM. As shown in Fig. 1(a), the measured root-mean-square (RMS) roughness is $\sim$ 0.467 nm, indicating a smooth and uniform surface. Such low roughness benefits heterostructure construction and magnon transport measurements.

The Morin phase transition is clearly observed in our α-Fe_2O_3 films. First, we cool the film from 300 K to 150 K without applying a magnetic field. Then, a constant external magnetic field of 5 kOe is applied in the film plane during the magnetization measurement as the temperature increases from 150 K to 350 K with an increment of 5 K. The temperature-dependent magnetization curve is shown in Fig. 1(b). The magnetization begins to rise around $\sim$ 235 K, followed by an abrupt increase as the film continues to heat up. The maximum slope of the change in magnetization is identified as a peak in the temperature-dependent dM/dT curve, located at $\sim$ 250 K. This sudden change in magnetization corresponds to the Morin phase transition of α-Fe_2O_3 film.[31–33] Therefore, this result reveals that the Morin temperature (T_M) of our 50-nm α-Fe_2O_3 film is approximately 250 K, which is close to the T_M value of the bulk α-Fe_2O_3 ($\sim$ 260 K).[34] This confirms that our sputtered α-Fe_2O_3 film possesses the expected antiferromagnetic properties. The slight reduction in the Morin temperature is attributed to the low dimensionality of thin films.[35,36]

To further identify the film quality, we perform Raman spectroscopy and XRD measurements. Figure 1(c) shows the Raman spectrum of the Pt/α-Fe_2O_3 heterostructure grown on the Al_2O_3 (0006) substrate at room temperature. The sample exhibits Raman peaks at approximately 227 cm^{-1}, 245 cm^{-1}, 296 cm^{-1}, 409 cm^{-1}, 496 cm^{-1}, 610 cm^{-1}, 656 cm^{-1}, 815 cm^{-1}, and 1311 cm^{-1} (denoted by the red solid boxes), which align well with the characteristic peaks of single-crystal α-Fe_2O_3 film.[37–41] The peak at 1311 cm^{-1} is associated with two-magnon scattering, further confirming the antiferromagnetic order of our film.[41] The absence of impurity-related Raman peaks consolidates high phase purity of the α-Fe_2O_3 and Pt/α-Fe_2O_3 heterostructure.

Figure 1(d) shows the XRD pattern for the same Al_2O_3 (0006) sub./Pt (10 nm)/α-Fe_2O_3 (50 nm) heterostructure. Two characteristic diffraction peaks are observed at 39.68° and 41.76°, respectively. The peak at 41.76° corresponds to the Al_2O_3 (0006) plane. According to previous reports, the XRD peak for the Pt (111) plane is at 39.6°, while the epitaxial α-Fe_2O_3 (0006) thin film is at 38.83°.[1] Since these two peaks are very close to each other, the peak at 39.68° in our sample cannot unambiguously be assigned solely to the epitaxial α-Fe_2O_3 (0006) layer. We attribute this peak to the combined diffraction contribution from the epitaxial Pt (111) and α-Fe_2O_3 (0006) bilayer.

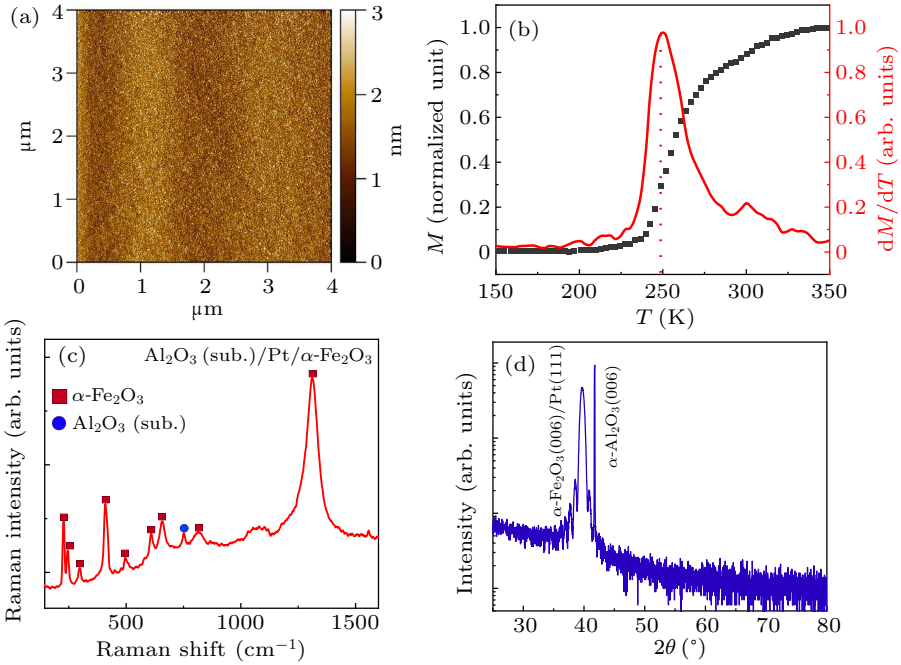


Fig. 1. (a) The AFM image of the α-Fe_2O_3 (50 nm) epitaxial film prepared under the optimized condition of $Ar : O_2 = 19.2 : 0.8$. (b) The temperature dependence of the magnetization M and dM/dT of a 50-nm α-Fe_2O_3 film while heating from 150 K to 350 K under a 5 kOe magnetic field. (c) Raman spectra and (d) XRD pattern of Al_2O_3 sub./Pt/α-Fe_2O_3 heterostructure, the thickness of α-Fe_2O_3 is 50 nm, and the thickness of Pt is 10 nm.

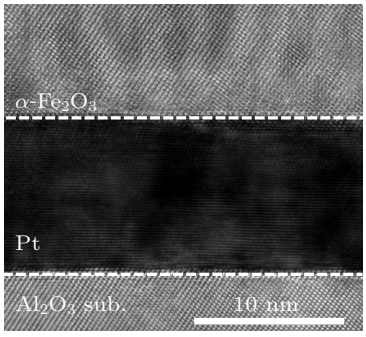


Fig. 2. High-resolution TEM images of Al_2O_3 sub./Pt/α-Fe_2O_3.

To clarify the epitaxial growth of the Pt/α-Fe_2O_3 heterostructure, high-resolution TEM measurements are performed. Figure 2 shows the TEM image of the Al_2O_3 (0006) sub./Pt (10 nm)/α-Fe_2O_3 (50 nm) heterostructure. The interface between Pt and α-Fe_2O_3 is clearly defined. Both the Pt and α-Fe_2O_3 lattices align neatly along the c-axis and match the substrate's crystal phase. Our highresolution TEM results further confirm the high epitaxial quality of the Pt/α-Fe_2O_3 heterostructure.

We deposit a 6-nm $Ni_{81}Fe_{19}$ (Py) layer on top of the epitaxial Pt (6 nm)/α-Fe_2O_3 (0006) bilayer and fabricate ST-FMR devices. Magnon transport and magnon torque can be characterized through ST-FMR measurement, which is an effective method for quantifying spin-torque efficiency. Figure 3(a) illustrates the ST-FMR measurement configuration. A radio-frequency current I_{RF} is applied to the ST-FMR device, generating spin accumulations at the Pt/α-Fe_2O_3 interface, with the spin polarization indicated by the red arrow. These spins interact with the nearby magnetic moments in the antiferromagnetic insulator α-Fe_2O_3 through s–d exchange coupling and induce a magnon current (J_M)[42] in the α-Fe_2O_3 layer. As

magnons transmit through the α-Fe_2O_3 layer, they can exert a magnon torque on the adjacent Py layer. Consequently, the precession of Py magnetization can give rise to the ST-FMR signal. Figure 3(b) shows the measured ST-FMR signals at different frequencies f ranging from 6 GHz to 11 GHz for the device with 20-nm α-Fe_2O_3. The ST-FMR data of some samples with different thicknesses of α-Fe_2O_3 are shown in Fig. S4. As shown in Fig. 3(c), the f as a function of the resonant magnetic field H_0 for different α-Fe_2O_3 thicknesses matches well with the Kittel formula. A representative $V_{\rm mix}$ signal (open symbols in Fig. 3(d)) from a device with $t_{\alpha-Fe_2O_3}$ of 20 nm is fitted by $V_{\rm mix} = V_{\rm S}F_{\rm S} + V_{\rm A}F_{\rm A}$, where $V_{\rm S}F_{\rm S}$ and $V_{\rm A}F_{\rm A}$ are the symmetric Lorentzian and antisymmetric Lorentzian components, respectively. By employing the well-established analysis methods,[43–45] we successfully evaluated the values of spin torque efficiency θ_i (i.e., electrical spin torque or magnon torque) for devices with varying α-Fe_2O_3 thicknesses from the symmetric components.

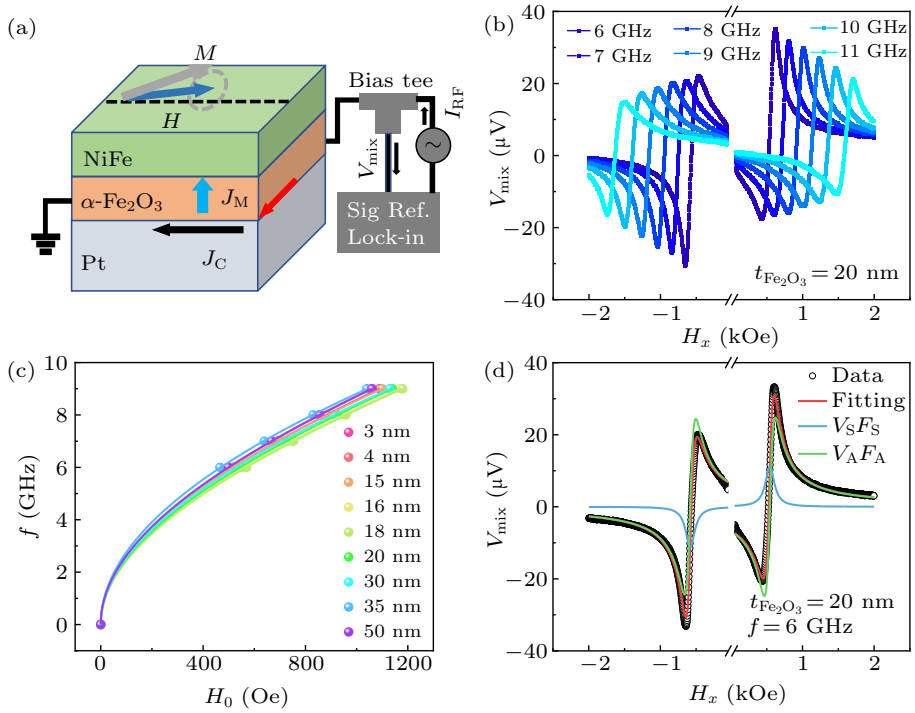


Fig. 3. (a) A schematic diagram of the ST-FMR measurements, illustrating the magnetization precession driven by the magnon torque. The black arrow denotes the $I_{\rm RF}$ with a current density $J_{\rm C}$. The red and blue arrows indicate the spin polarizations and magnon current $J_{\rm M}$, respectively. (b) The ST-FMR signals of Pt/α-Fe_2O_3 (20 nm)/Py (6 nm) device at different frequencies. (c) Resonance frequency f against the resonant field H for Pt (6 nm)/α-Fe_2O_3 (t nm)/Py (6 nm) devices with fits (solid lines). (d) A typical ST-FMR signal (open symbols) from a Pt (6 nm)/α-Fe_2O_3 (20 nm)/Py (6 nm) device at 6 GHz and 300 K with fits (solid lines).

Figure 4(a) illustrates the dependence of spin torque efficiency θ_i on the α-Fe_2O_3 thickness for various devices at room temperature. It is important to note that θ_i originates either from the electrical spin torque associated with electron spins (i = S) or from the magnon torque linked to the magnons (i = M), depending on the thickness of the α-Fe_2O_3 layer, as will be discussed later. For devices without an α-Fe_2O_3 layer (i.e., Pt/Py bilayers), θ_i is evaluated to be ~ 0.06. This is consistent with the previously reported value for the heavy metal Pt.[46] When a 2-nm α-Fe_2O_3 layer is inserted between the Pt and Py layers, θ_i abruptly drops to ~ 0.018. As shown in the left panel of Fig. 4(b), this spin torque can be attributed to the purely electron spins from the Pt layer (i.e., spin–orbital torque), which tunnel through the thin insulating α-Fe_2O_3 layer. This process is similar to electron tunneling through typical insulators, such as MgO or SiO_2 layers.[47,48] As the thickness of the α-Fe_2O_3 layer increases, θ_i further decreases and eventually approaches nearly zero at $t_{\alpha-Fe_2O_3}$ of 10 nm. At this point, electron spins are almost completely blocked by the insulating α-Fe_2O_3. In this regime, the antiferromagnetic order of the α-Fe_2O_3 layer has not yet been established, and the contribution from magnon torque remains negligible.

Magnon torque is observed in devices with a thicker α-Fe_2O_3 layer. In such cases, the insulating α-Fe_2O_3 layer becomes too thick to allow electron spins to tunnel through; therefore, magnons are the only carriers of spin-angular momentum, as shown in the right panel of Fig. 4(b). It is found that θ_i starts to increase when the α-Fe_2O_3 thickness exceeds 15 nm, peaks at 20 nm with a value of ~ 0.047, and then gradually decreases as the thickness of the α-Fe_2O_3 layer further increases up to 50 nm. The observed increase in θ_i clearly evidences the contribution of magnon torque.

This non-monotonic behavior of θ_i, with a distinct peak at $t_{\alpha-Fe_2O_3} = 20$ nm, suggests that the magnon transport efficiency depends critically on the evolution of antiferromagnetic order and crystallinity within the α-Fe_2O_3 layer. To ver-

ify this hypothesis, we performed complementary characterizations of representative ST-FMR devices. The long-range antiferromagnetic order can be indicated by the interfacial exchange bias field (H_{EB}), which increases as the antiferromagnetic order improves.[49] Exchange bias measurements (supplemental materialS3, Fig. S5) show that H_{EB} is negligible for thicknesses $\leq$ 16 nm, but emerges and increases for $t_{\alpha-Fe_2O_3}$ = 18 nm and 20 nm. This indicates that the antiferromagnetic order of α-Fe_2O_3 progressively strengthens with increasing thickness. Furthermore, we provide a high-resolution cross-sectional TEM image of the device with a 20-nm-thick α-Fe_2O_3 layer (Fig. S6). The image reveals a highly ordered epitaxial structure, directly confirming the high crystal quality of the α-Fe_2O_3 film at this thickness. These findings provide direct evidence that the concurrent enhancement of antiferromagnetic order and crystal quality establishes an efficient, low-scattering channel for magnon diffusion, thereby leading to the observed peak in torque efficiency in devices with 20-nm α-Fe_2O_3.

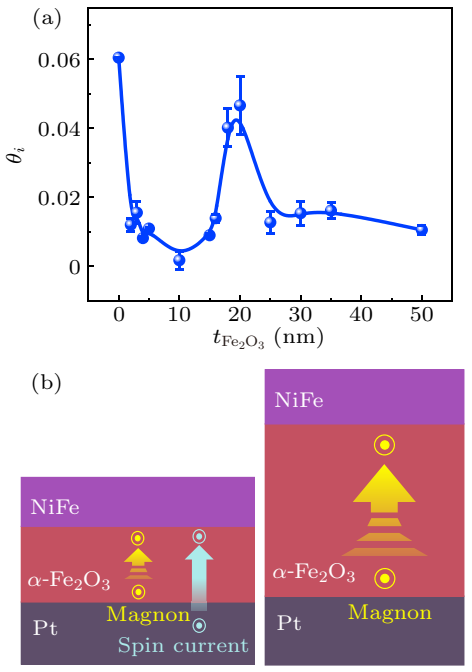


Fig. 4. (a) The α-Fe_2O_3 thickness-dependent spin torque θ_i at 300 K. (b) Schematic diagram showing magnon-only torque (right panel) and spin-dominated torques (left panel). When the thickness of α-Fe_2O_3 is thin, electron spin transmission through α-Fe_2O_3 is dominant, but when α-Fe_2O_3 is thick, only magnons can be transmitted through it.

The nonzero torque efficiency observed at large thicknesses (e.g., 50 nm) raises the question of whether contributions beyond magnon transport, such as those from the α-Fe_2O_3/NiFe interface, are present. To address this, we performed control experiments on devices without Pt layer [i.e., α-Fe_2O_3 (50 nm)/NiFe]. ST-FMR measurements on such a control device yield a small spin torque efficiency of $\sim$ 0.005. This value represents the intrinsic interfacial contribution (θ_{int}) at the α-Fe_2O_3/NiFe interface. Through a detailed analysis (supplemental material S4), we extracted the pure magnon torque contribution transmitted through a 50-nm-thick α-Fe_2O_3 bulk (θ_{bulk}), which is negligible at approximately 0.0043. This result confirms the existence of a weak interfacial contribution that is largely independent of α-Fe_2O_3 thickness.

The distinct magnon torque effect observed in devices with an antiferromagnetic insulator α-Fe_2O_3 is attributed to an enhanced magnon transmission efficiency. The magnon transmission efficiency, η, is defined as the ratio of θ_i ($t_{\alpha-Fe_2O_3}$ = 20 nm)/θ_i ($t_{\alpha-Fe_2O_3}$ = 0 nm). Notably, the magnon transmission efficiency in our devices reaches $\sim$ 75%, which is 2.5 times higher than that previously reported for the antiferromagnetic insulator NiO.[20,50] We attribute this enhancement of η to the better antiferromagnetic ordering at room temperature and the higher epitaxial quality of α-Fe_2O_3 film. The lower density of crystal defects and grain boundaries in the film reduces the probability of magnon scattering, thereby enabling more efficient magnon transport through the α-Fe_2O_3 layer.

In addition, we discuss other possible contributions of temperature, interfacial spin transparency, and magnon coherence to magnon transport through α-Fe_2O_3 in our system. It is known that in antiferromagnetic insulators such as NiO, magnon-transport efficiency peaks near the Néel temperature (T_N).[51–54] However, this mechanism is not the primary driver of the high room-temperature efficiency observed here. Bulk α-Fe_2O_3 possesses a high T_N of $\sim$ 950 K, and even in thin-film form its magnetic order remains robust well above room temperature. Therefore, our experiments at 300 K operate in a regime far below T_N, where the magnon-transport efficiency is less susceptible to thermal fluctuations.

We next address the possible influence of interfacial spin transparency. The spin transparency T for Pt/α-Fe_2O_3(15, 20, 25, 50 nm)/NiFe was analyzed. First, based on the measured ST-FMR data, the Gilbert damping constant α was extracted using the following relation:[55]

$$\Delta = \Delta_0 + \frac{2\pi\alpha}{\gamma} f, \tag{1}$$

where γ is the gyromagnetic ratio, f is the frequency of the radio-frequency (RF) current, and Δ is the extrinsic contribution to the linewidth. The T was subsequently obtained using the following equations:[55–57]

$$g_{\text{eff}}^{\uparrow\downarrow} = \frac{4\pi M_S t_{FM}}{g\mu_B}(\alpha - \alpha_{FM}), \tag{2}$$

$$T = \frac{g_{\text{eff}}^{\uparrow\downarrow} \tanh\frac{t_{Pt}}{2\lambda_{Pt}}}{g_{\text{eff}}^{\uparrow\downarrow} \coth\frac{t_{Pt}}{\lambda_{Pt}} + \frac{\sigma_{Pt} h}{\lambda_{Pt} 2e^2}}, \tag{3}$$

where g_{eff} represents the absorption of transverse spin current at the Pt/NiFe interface. α denotes the damping constant for the Pt/α-Fe_2O_3/NiFe heterostructure, and α_{FM} represents the damping constant for the reference ferromagnetic film. The

resulting T values are $T \approx 0.5783$ ($t_{\alpha-Fe_2O_3} = 15$ nm), 0.6078 ($t_{\alpha-Fe_2O_3} = 20$ nm), 0.5264 ($t_{\alpha-Fe_2O_3} = 25$ nm), and 0.5814 ($t_{\alpha-Fe_2O_3} = 50$ nm). These values all lie within a narrow range and show no strong correlation with thickness. Therefore, our observed thickness dependence of magnon torque cannot be attributed to the variations in interfacial spin transparency.

In our system, magnons are generated via the electrical injection of spin-polarized currents into the antiferromagnetic layer. Such electrically excited magnon populations are inherently incoherent, as they are created in a non-equilibrium state with random phases.[4,58–60] Consequently, the transport of these magnons is well described by a diffusive, rather than coherent, propagation model. In the diffusive regime, transmission efficiency is not governed by phase interference but is fundamentally limited by scattering processes. Therefore, the mean free path and relaxation time of magnons — and ultimately the overall transmission efficiency — critically depend on the crystal quality (which minimizes defect scattering)[58] and the robustness of the antiferromagnetic order. This is consistent with our conclusion that the enhanced magnon-transport efficiency originates from the superior crystal quality and antiferromagnetic order of the epitaxial α-Fe_2O_3 thin films. Therefore, the primary determinant of the observed high magnon-transport efficiency is the combination of antiferromagnetic order and high crystallinity achieved in our epitaxial α-Fe_2O_3 films at room temperature.

4. Conclusion

In summary, we successfully grow an epitaxial α-Fe_2O_3 thin film and Pt/α-Fe_2O_3 heterostructures using high-vacuum magnetron sputtering, which is compatible with semiconductor manufacturing. The α-Fe_2O_3 thin films show strong antiferromagnetic order with a Morin temperature of 250 K. We observe efficient magnon transport and magnon torque in the Pt/α-Fe_2O_3/Py devices. The magnon transmission efficiency is $\sim 75\%$ through the epitaxial α-Fe_2O_3 layer, surpassing previously reported NiO-based magnon torque devices by a factor of 2.5. This work demonstrates that the antiferromagnetic insulator α-Fe_2O_3, with a higher Néel temperature and improved crystallization, is a promising material for magnon transfer and enables larger magnon torque.

Acknowledgements

Project supported by the National Natural Science Foundation of China (Grant Nos. T2495211, 12261131506, 12074052, and 12504121), the Natural Science Foundation of Liaoning Province of China (Grant Nos. 2021-YQ-06 and 2025-BS-0077), the Open Fund of the State Key Laboratory of Spintronics Devices and Technologies (Grant No. SPL-2410), and the Fundamental Research Funds for the Central Universities (Grant Nos. DUT24GJ204, DUT25Z2746, and DUT25RC(3)066). The authors acknowledge Shuyan Shi, Jingyi Xiao, and Xiaoxia Gao and Na Ta from the Experimental Center of the Material Science and Engineering Department and the DUT Instrumental Analysis Center, for their assistance with sample characterizations.

References

[1] Jungwirth T, Sinova J, Manchon A, Marti X, Wunderlich J and Felser C 2018 *Nat. Phys.* **14** 200
[2] Kajiwara Y, Harii K, Takahashi S, Ohe J I, Uchida K, Mizuguchi M, Umezawa H, Kawai H, Ando K, Takanashi K, Maekawa S and Saitoh E 2010 *Nature* **464** 262
[3] Han X, Wu H and Zhang T 2024 *Appl. Phys. Lett.* **125** 020501
[4] Lebrun R, Ross A, Bender S A, Qaiumzadeh A, Baldrati L, Cramer J, Brataas A, Duine R A and Kläui M 2018 *Nature* **561** 222
[5] Chumak A V, Vasyuchka V I, Serga A A and Hillebrands B 2015 *Nat. Phys.* **11** 453
[6] Cheng R, Xiao D and Brataas A 2016 *Phys. Rev. Lett.* **116** 207603
[7] Wang Q, Csaba G, Verba R, Chumak A V and Pirro P 2024 *Phys. Rev. Appl.* **21** 040503
[8] Gasemi S and Ebrahimkhas M 2025 *Chin. Phys. B* **34** 077302
[9] Guo X, Zhang M and Yao D 2025 *Chin. Phys. Lett.* **42** 120703
[10] Zhu H, Shi H, Tang Z and Tang B 2024 *Chin. Phys. B* **33** 037503
[11] Rezende S M, De Aguiar F M and Azevedo A 2006 *Phys. Rev. B* **73** 094402
[12] Yu H, d'Allivy Kelly O, Cros V, Bernard R, Bortolotti P, Anane A, Brandl F, Heimbach F and Grundler D 2016 *Nat. Commun.* **7** 11255
[13] Demidov V E, Urazhdin S, Ulrichs H, Tiberkevich V, Slavin A, Baither D, Schmitz G and Demokritov S O 2012 *Nat. Mater.* **11** 1028
[14] Cornelissen L J, Liu J, Duine R A, Youssef J B and Van Wees B J 2015 *Nat. Phys.* **11** 1022
[15] Evelt M, Soumah L, Rinkevich A B, Demokritov S O, Anane A, Cros V, Ben Youssef J, de Loubens G, Klein O, Bortolotti P and Demidov V E 2018 *Phys. Rev. Appl.* **10** 041002
[16] Lin W, Chen K, Zhang S and Chien C L 2016 *Phys. Rev. Lett.* **116** 186601
[17] Qiu Z, Hou D, Barker J, Yamamoto K, Gomonay O and Saitoh E 2018 *Nat. Mater.* **17** 577
[18] Yuan W, Zhu Q, Su T, Yao Y, Xing W, Chen Y, Ma Y, Lin X, Shi J, Shindou R, Xie X C and Han W 2018 *Sci. Adv.* **4** eaat1098
[19] Wang W, Wang T, Amin V P, Wang Y, Radhakrishnan A, Davidson A, Allen S R, Silva T J, Ohldag H, Balzar D, Zink B L, Haney P M, Xiao J Q, Cahill D G, Lorenz V O and Fan X 2019 *Nat. Nanotechnol.* **14** 819
[20] Wang Y, Zhu D, Yang Y, Lee K, Mishra R, Go G, Oh S H, Kim D H, Cai K, Liu E, Pollard S D, Shi S, Lee J, Teo K L, Wu Y, Lee K J and Yang H 2019 *Science* **366** 1125
[21] Guo C Y, Wan C H, Zhao M K, Fang C, Ma T Y, Wang X, Yan Z R, He W Q, Xing Y W, Feng J F and Han X F 2021 *Phys. Rev. B* **104** 094412
[22] Wang F, Shi G, Yang D, Tan H R, Zhang C, Lei J, Pu Y, Yang S, Soumyanarayanan A, Elyasi M and Yang H 2024 *Nat. Nanotechnol.* **19** 1478
[23] Zheng D, Tang M, Xu J, Liu C, Li Y, Chen A, Algaidi H, Alsayafi F, Chen M, Ma Y, Zhang S, Zhang L, Li P and Zhang X 2024 *Appl. Phys. Lett.* **124** 102406
[24] Wang Y and Yang H 2022 *Acc. Mater. Res.* **3** 1061
[25] Yi W 2020 *Physics* **49** 29
[26] Shi G, Wang F, Tan H R, Zhao S, Liu Y, Yang D, Lee K, Pu Y, Yang S, Soumyanarayanan A and Yang H 2023 *Phys. Rev. Appl.* **19** 034039
[27] Ohmichi E, Shoji Y, Takahashi H and Ohta H 2022 *J. Phys. Soc. Jpn.* **91** 095001
[28] Chen X, Jarvis K, Sullivan S, Li Y, Zhou J and Shi L 2017 *Phys. Rev. B* **95** 144310
[29] Wang J, Wu W, Zhao F and Zhao G M 2011 *J. Appl. Phys.* **109** 056101
[30] Tanner B K, Clark G F and Safa M 1988 *Philos. Mag. B* **57** 361
[31] Pati S P, Al-Mahdawi M, Ye S, Nozaki T and Sahashi M 2017 *Phys. Status Solidi RRL* **11** 1700101
[32] Shimomura N, Pati S P, Sato Y, Nozaki T, Shibata T, Mibu K and Sahashi M 2015 *J. Appl. Phys.* **117** 17
[33] Bhowmik R N and Saravanan A 2010 *J. Appl. Phys.* **107** 053916
[34] Morin F J 1950 *Phys. Rev.* **78** 819

[35] Cao M, Liu T, Gao S, Sun G, Wu X, Hu C and Wang Z L 2005 *Angew. Chem., Int. Ed.* **44** 4197
[36] Kim C H, Chun H J, Kim D S, Kim S Y, Park J, Moon J Y, Lee G, Yoon J, Jo Y, Jung M H, Jung S I and Lee C J 2006 *Appl. Phys. Lett.* **89** 223103
[37] de Faria D L A, Venâncio Silva S and de Oliveira M T 1997 *Journal of Raman spectroscopy* **28** 873
[38] Fu Y Y, Wang R M, Xu J, Chen J, Yan Y, Narlikar A V and Zhang H 2003 *Chem. Phys. Lett.* **379** 373
[39] Beattie I R and Gilson T R 1970 *J. Chem. Soc. A* 980
[40] McCarty K F 1988 *Solid State Commun.* **68** 799
[41] Bersani D, Lottici P P and Montenero A 1999 *Journal of Raman Spectroscopy* **30** 355
[42] Zhang S S L and Zhang S 2012 *Phys. Rev. B* **86** 214424
[43] Mellnik A R, Lee J S, Richardella A, Grab J L, Mintun P J, Fischer M H, Vaezi A, Manchon A, Kim E A, Samarth N and Ralph D C 2014 *Nature* **511** 449
[44] Wang Y, Deorani P, Banerjee K, Koirala N, Brahlek M, Oh S and Yang H 2015 *Phys. Rev. Lett.* **114** 257202
[45] Wang Y, Ramaswamy R and Yang H 2018 *J. Phys. D: Appl. Phys.* **51** 273002
[46] Wang Y, Deorani P, Qiu X, Kwon J H and Yang H 2014 *Appl. Phys. Lett.* **105** 152412
[47] Hahn C, de Loubens G, Naletov V V, Ben Youssef J, Klein O and Viret M 2014 *Europhys. Lett.* **108** 57005
[48] Wang H, Du C, Hammel P C and Yang F 2014 *Phys. Rev. Lett.* **113** 097202
[49] Nogués J and Schuller I K 1999 *J. Magn. Magn. Mater.* **192** 232
[50] Shi G, Wang F, Tan H R, Zhao S, Liu Y, Yang D, Lee K, Pu Y, Yang S and Soumyanarayanan A 2023 *Phys. Rev. Appl.* **19** 034039
[51] Lin W, Chen K, Zhang S and Chien C 2016 *Phys. Rev. Lett.* **116** 186601
[52] Hou D, Qiu Z, Barker J, Sato K, Yamamoto K, Vélez S, Gomez-Perez J M, Hueso L E, Casanova F and Saitoh E 2017 *Phys. Rev. Lett.* **118** 147202
[53] Qiu Z, Li J, Hou D, Arenholz E, N'Diaye A T, Tan A, Uchida K I, Sato K, Okamoto S, Tserkovnyak Y, Q Q Z and Saitoh E 2016 *Nat. Commun.* **7** 12670
[54] Prakash A, Brangham J, Yang F and Heremans J P 2016 *Phys. Rev. B* **94** 014427
[55] Yang P, Shao Q, Yu G, He C, Wong K, Lu X, Zhang J, Liu B, Meng H, He L, Wang K L and Xu Y 2020 *Appl. Phys. Lett.* **117** 082409
[56] Zhang W, Han W, Jiang X, Yang S H and SP Parkin S 2015 *Nat. Phys.* **11** 496
[57] Pai C F, Ou Y, Vilela-Leão L H, Ralph D C and Buhrman R A 2015 *Phys. Rev. B* **92** 064426
[58] Xing W, Qiu L, Wang X, Yao Y, Ma Y, Cai R, Jia S, Xie X and Han W 2019 *Phys. Rev. X* **9** 011026
[59] Das S, Ross A, Ma X X, Becker S, Schmitt C, Van Duijn F, Galindez-Ruales E F, Fuhrmann F, Syskaki M A, Ebels U, Baltz V, Barra A L, Chen H Y, Jakob G, Cao S X, Sinova J, Gomonay O, Lebrun R and Kläui M 2022 *Nat. Commun.* **13** 6140
[60] de Wal D K, Iwens A, Liu T, Tang P, Bauer G E and van Wees B J 2023 *Phys. Rev. B* **107** 1